GDCh Research Article Angewandte International Edition Chemie www.angewandte.org

How to cite: Angew. Chem. Int. Ed. 2025, e202421547
doi.org/10.1002/anie.202421547

Indoor Photovoltaics Hot Paper

6H-Intermediate Phase Enabled Slow Crystal Growth of Tin Halide Perovskites for Indoor Photovoltaics

*Muhammad Abdel-Shakour[+], Junfang Wang[+], Junjie Huang, Zhen Gao, Yongle Pan, and Xiangyue Meng**

Abstract: The rapid expansion of Big Data and Internet of Things (IoT) has driven significant advancements in indoor photovoltaics (IPVs), which provide power to wireless IoT devices. Tin halide perovskites (THPs) have garnered significant attention for IPVs due to their excellent optoelectronic properties without the environmental risks of lead exposure. However, THPs face challenges in controlling their fast crystallization process. Here, we introduce a novel approach to precisely control the crystallization kinetics of $FASnI_2Br$ perovskite via the formation of the 6H-intermediate phase, supported by the mesomeric (+M) interaction effect of 4-aminopyridine hydrochloride (4APCl) in the perovskite precursor. The grazing-incidence wide-angle X-ray scattering measurements indicated the formation of 6H-intermediate phase for the $FASnI_2Br$-4APCl perovskite during the crystallization process. The in situ ultraviolet-visible absorption spectroscopy during the spin coating and annealing process confirmed the reduction of crystal growth rate after the 6H-intermediate phase formation. Thus, high-quality perovskite films were obtained with reduced defects. The resulting IPVs achieved an efficiency of 21.55 % under indoor illumination at 1000 lux, exceeding all types of lead-free perovskite IPVs.

Introduction

Indoor photovoltaics (IPVs) are gaining prominence as a viable energy source in urban and indoor settings, where traditional solar applications are less feasible. Recent advances highlight their role in powering low-energy devices for the Internet of Things (IoT), improving energy efficiency and reducing costs.[1–4] The IPV market is anticipated to experience a significant expansion, driven by increasing demand for smart building solutions that enhance both energy generation and indoor design.[5–7] Indoor lighting sources, such as fluorescent lamps and light emitting diodes, emit in the 400 to 700 nm range. Materials with a band gap between 1.7 and 1.9 eV are ideal for absorbing indoor light.[8–10] However, the lower band gap of 1.12 eV makes silicon solar cells less efficient at harvesting indoor light, which is not suitable for IPV applications.[9,11,12]

Various wide band gap materials, such as dye molecules, organic semiconductors, and halide perovskites, are being explored for IPVs.[10,13,14] Particularly, perovskites have shown significant promise due to their high light absorption and energy conversion efficiency.[15–17] The wide band gap perovskite solar cells (PSCs) have achieved a power conversion efficiency (PCE) up to 43 % for indoor photovoltaic applications.[18–22] Nevertheless, their reliance on toxic lead presents a health risk, because indoor IoT devices operate in close proximity to people, unlike traditional solar panels, which are usually placed far from human contact.[23–25] Fortunately, tin halide perovskites (THPs) offer outstanding characteristics for IPV applications, such as lower toxicity compared to Pb analogous, a tunable band gap, high charge carrier mobility, and a long lifetime of hot carriers.[26–30] However, the crystallization process of wide band gap THPs is primarily influenced by the high Lewis acidity of divalent Sn halides, in addition to the increased Br content.[31–34] Consequently, the crystallization process is accelerated with the formation of numerous defects in the wide band gap THPs.[35–39] These defects facilitate the formation of non-radiative recombination centers, thereby reducing open-circuit voltage (V_{oc}) under indoor light illumination.[10,40–42] To boost the PCE of indoor Sn-PSCs, Liao et al. introduced catechin Lewis base additive in the $FA_{0.75}MA_{0.25}SnI_2Br$ perovskite precursor. Via the hydroxyl group, catechin interacted with the perovskite precursor and successfully controlled the crystal growth. Consequently, a PCE of 12.81 % under 1000 lux was achieved.[43] To optimize the energy level at the hole transport layer (HTL)/perovskite interface, the PEDOT:PSS HTL was treated with nicotinamide. The nicotinamide-modified PEDOT:PSS exhibited lower interfacial defects and minimized V_{oc} loss, yielding a PCE of 14.40 % under 1000 lux LED illumination.[44] Further improvements were achieved by including a KSCN interlayer between the PEDOT:PSS layer and $FA_{0.75}MA_{0.25}SnI_2Br$, which promoted the crystallization process and the interfacial carrier transport. As result, a high PCE of 17.57 % under 2956 K @1062 lux was obtained.[45] Recently, our group incorporated CsF into the

[*] M. Abdel-Shakour,[+] J. Wang,[+] J. Huang, Z. Gao, Y. Pan, Prof. X. Meng
School of Optoelectronics, Center of Materials Science and Optoelectronics Engineering, University of Chinese Academy of Sciences, Beijing, 100049, China
E-mail: mengxiangyue@ucas.ac.cn
M. Abdel-Shakour[+]
Chemistry Department, Faculty of Science, Assiut University, Assiut, 71516, Egypt
[+] These authors contributed equally

PEDOT:PSS layer to tune the adhesive bonding strength of the buried interfaces.[46] The perovskite film based on CsF-modified PEDOT:PSS achieved an enhanced nucleation rate, which reduced defects and improved surface morphology. Notably, a PCE of 20.12 % under 1000 lux indoor light was reported.[46]

Despite numerous efforts have been devoted for enhancing the PCE of wide band gap THPs for IPVs, the crystallization process of wide band gap THPs is still challenging to control due to the rapid interaction of divalent tin halides in the perovskite precursor.[47,48] The uncontrolled crystallization process produces perovskite films with pinholes and a high defect density, which subsequently increases the V_{oc} loss of the target IPVs.[18,36, 49] Unlike previous strategies, we demonstrate a novel approach for controlling the crystal growth of wide band gap THPs by establishing the 6H-intermediate phase during the formation of perovskite films. The inclusion of 4-aminopyridine hydrochloride (4APCl) in the perovskite precursor promoted the formation of 6H-intermediate phase, aided by the positive mesomeric (+M) interaction between 4APCl and perovskites.[50,51] The grazing-incidence wide-angle X-ray scattering (GIWAXS) measurements revealed the formation of the 6H-intermediate perovskite phase after the inclusion of 4APCl, thereby facilitating the slowed crystal growth of THPs.[52] The in situ ultraviolet-visible (UV/Vis) absorption spectroscopy during the spin coating and annealing process proved the reduction in crystal growth rate after the 6H-intermediate phase formation. We propose that the reduction in crystallization rate is primarily attributable to the stabilization of the 6H-intermediate phase through the robust interaction between 4APCl and the perovskite precursor during the crystallization process-a synergistic effect. Thus, high-quality perovskite films with enhanced crystallinity, reduced lattice strain, suppressed defects and recombination centers were obtained. The fabricated IPVs based on $FASnI_2Br$-4APCl exhibited a PCE of 21.55 % compared to 15.18 % for the pristine $FASnI_2Br$ devices under indoor light illumination (3000 K, 1000 lux). To the best of our knowledge, this is the highest reported PCE for indoor photovoltaics based on lead-free perovskites.

Results and Discussion

The structural characteristics of the wide band gap THP films are significantly influenced by the crystal growth kinetics.[53,54] Usually, the crystal growth of THPs occurs rapidly due to the high Lewis acidity of divalent tin halides.[55,56] The rapid crystal growth of the perovskite precursors results in THP films characterized by inferior morphology with the presence of pinholes and defects, thereby leading to poor photovoltaic performance of Sn-PSCs. Importantly, the formation of a meta-stable intermediate phase can reduce the rapid crystal growth rate of THPs.[56–58] Herein, we introduced aminopyridine isomers as additives into the perovskite precursor in order to slow down the crystal growth rate via the formation of an intermediate phase.

The basicity of aminopyridine isomers is primarily influenced by the nitrogen atom located on the pyridine ring and the external amine group. The pKa value of aromatic pyridine is 5.5, which is significantly higher than aniline (4.6).[59] The delocalization of the lone electron pair from the external amine group into the π-system of the aromatic ring enhances the ability of aminopyridines for electron donation.[60,61] From a chemical perspective, the bonding interaction between the amino group and the pyridine ring alters the electronic properties of aminopyridine isomers: 4-aminopyridine hydrochloride (4APCl), 2-aminopyridine hydrochloride (2APCl), and 3-aminopyridine hydrochloride (3APCl), leading to variations in their basicity. The lone pair on the nitrogen of the amino group is capable of either donating electrons to the nitrogen of the pyridine ring through a positive mesomeric (+M) effect, or pulling electrons away from the ring nitrogen through a negative inductive effect. Nevertheless, the mesomeric effect is stronger, rendering aminopyridines more basic than pyridines. The positive mesomeric effect of the exo-amine on 4-aminopyridine (4APy) increases the electron density on the ring nitrogen, thereby stabilizing the negative charge on the pyridine ring's nitrogen, as explained in Figure 1a.[62,63] Alternatively, the presence of steric hindrance and intramolecular hydrogen bonding, whereby hydrogen atoms from adjacent amine groups interact with the lone pair on the ring nitrogen, results in a decrease in the basicity of 2-amion pyridine (2APy) and 3-aminopyridine (3APy) in comparison to 4APy.[64] Consequently, the basicity of aminopyridine derivatives can be arranged as follows: 4APy ($pK_a = 9.17$) > 2APy ($pK_a = 6.86$) > 3APy ($pK_a = 6.00$), as shown in Figure 1b. More importantly, density functional theory (DFT) calculations indicated that the electrostatic potential (ESP) for 4APCl, 2APCl and 3APCl is −32.52, −26.41 and −28.86 kcal/mol, respectively. Thus, the 4APCl molecule exhibited the highest negative ESP value compared to pyridine and aminopyridine isomers, as explained in Figures 1c, S1. Consequently, the high electron density of 4APCl is expected to exhibit a strong interaction with the perovskite precursor, which is crucial for achieving slow crystal growth.

To clearly investigate the strong interaction between 4APCl and SnI_2 in the perovskite precursor, nuclear magnetic resonance (^{1}H NMR) spectroscopy of SnI_2-4APCl compared to 4APCl was measured. As shown in Figures 1d, S2a, the ^{1}H NMR peaks of SnI_2-4APCl exhibited an obvious chemical shift compared to the pristine 4APCl, indicating a strong interaction between SnI_2 and 4APCl. In order to gain further insight into the interaction mechanism between 4APCl and the perovskite precursor, we prepared the SnI_2-4APCl adduct (Figure S3). The interaction was further confirmed using Fourier-transform infrared (FTIR) spectroscopy. As indicated in Figures 1e, S2b, the N–H asymmetric and symmetric stretching vibrations of the amino group in the SnI_2-4APCl adduct were shifted from 3433 cm^{-1} to 3338 cm^{-1} and from 3298 cm^{-1} to 3288 and 3263 cm^{-1}, respectively, compared to the pristine 4APCl. Furthermore, the N–H in-plane deformation vibration was decreased from 1645 cm^{-1} to 1643 cm^{-1}. Additionally, the stretching vibra-

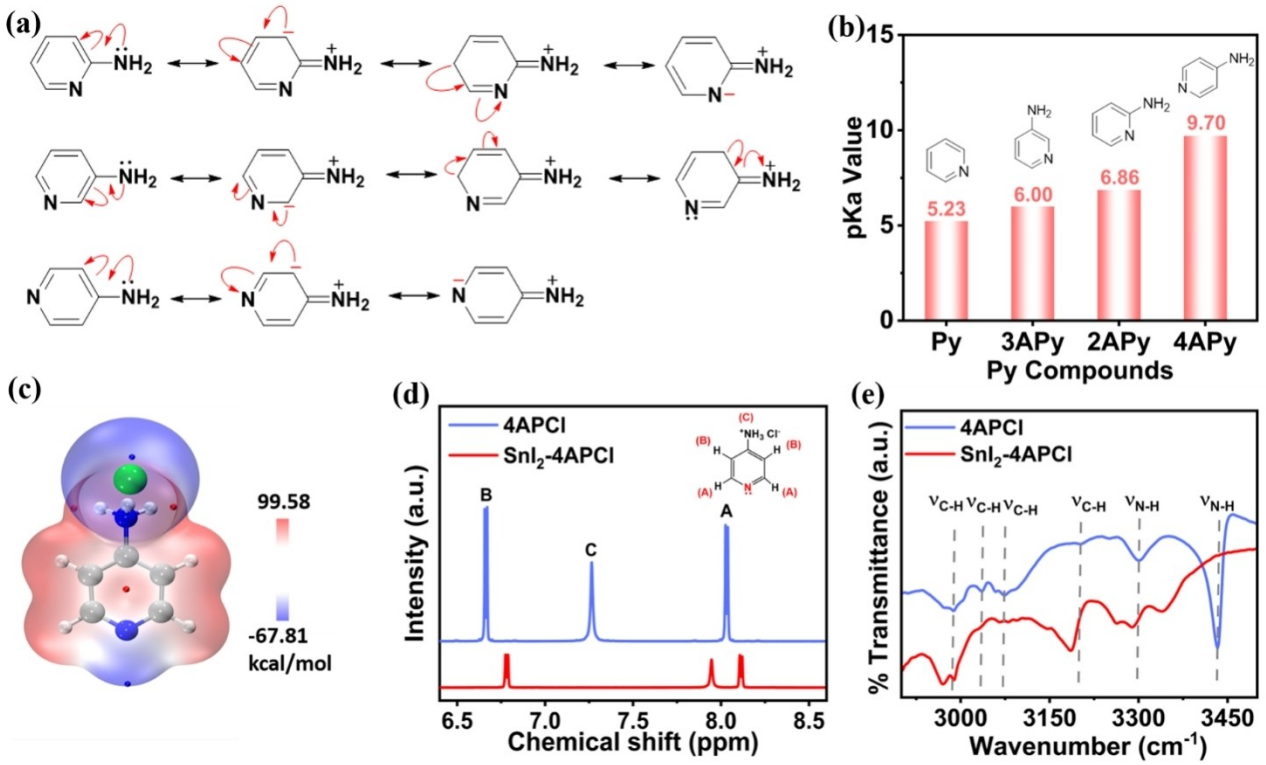

Figure 1. Basicity of aminopyridine isomers and their interaction with perovskites. (a) The influence of resonance structure on the basicity of aminopyridine isomers. (b) The pKa values of pyridine and aminopyridine isomers. (c) The electrostatic potential of 4APCl molecule. (d) ^{1}H NMR and (e) FTIR spectra of 4APCl with and without SnI_2.

tion of C=N in the pyridine ring shifted from 1595 cm^{-1} to 1580 cm^{-1} and the stretching vibration of C-NH_2 was shifted from 1267 cm^{-1} to 1207 cm^{-1} after introducing 4APCl.[65,66] The above analysis demonstrated the strong interaction between 4APCl and SnI_2, which is beneficial for regulating the crystal growth kinetics of wide band gap THPs. It is worth noting that the ^{1}H NMR spectrum of SnI_2+4APCl exhibited a pronounced chemical shift ($\Delta\delta = 0.68$) compared to SnI_2 mixed with 2APCl, 3APCl, and PyCl (Figure S4 and Table S1). This significant chemical shift can be attributed to the strong mesomeric interaction at the para position between the amino group and the nitrogen in the pyridine ring, which leads to the significant shift observed in the case of 4APCl. Therefore, the interaction of 4APCl with the perovskite precursor was stronger than that of 2APCl, 3APCl, and PyCl.

To better understand the effect of 4APCl on the crystallization of $FASnI_2Br$ perovskite films, GIWAXS measurements were performed on the perovskite films during the spin coating process. As depicted in Figure 2a, the intensity of the perovskite (001) peak at approximately $q_z = 1.015$ Å^{-1} was detected in the pristine $FASnI_2Br$ perovskite films, indicating the rapid formation of perovskite structure during the spin coating process. Notably, after the inclusion of 2 mol% 4APCl in the pristine $FASnI_2Br$ perovskite films, a new peak at $q_z = 0.98$ Å^{-1} was observed in the $FASnI_2Br$-4APCl perovskite film during the spin coating process (Figures 2b, d). This peak completely disappeared after annealing, as shown in Figures 2c, S5. In contrast, this new peak at $q_z = 0.98$ Å^{-1} couldn't be detected in the pristine $FASnI_2Br$ film during the spin coating or after the annealing process (Figures 2d, S5). The newly observed peak at $q_z = 0.98$ Å^{-1} could be attributed to the formation of the 6H-intermediate phase.[67,68] It was anticipated that the incorporation of 4APCl would enhance the formation of the 6H-intermediate phase due to the strong interaction between 4APCl and perovskite.[52] To confirm the formation of the 6H-intermediate phase, we prepared SnI_2-4APCl films with a molar ratio of 1:1 and measured the XRD patterns. As depicted in Figure 2e, the fingerprint peaks of the 6H-intermediate phase were observed at 14° and 12.12°, which is consistent with previous XRD results for the 6H-intermediate phase of lead halide perovskites. These findings agree with the GIWAXS results and further validate the formation of the 6H-intermediate phase during the crystallization of the $FASnI_2Br$-4APCl perovskite film. This is the first time that the 6H-intermediate phase has been observed in tin halide perovskite films, which is preferable for slowing down crystal growth. Figure 2f shows the possible arrangements and the connectivity of the SnI_6 octahedra of the 6H-intermediate phase.[52,67] The structure of the 6H-intermediate phase exhibits a large number of corner-sharing octahedra that can act as inter-grain growth channels by the intervening halides.[52] It was reported that the 6H-intermediate phase could help to reduce the crystal growth rate, while maintaining the homogeneity and integrity of the

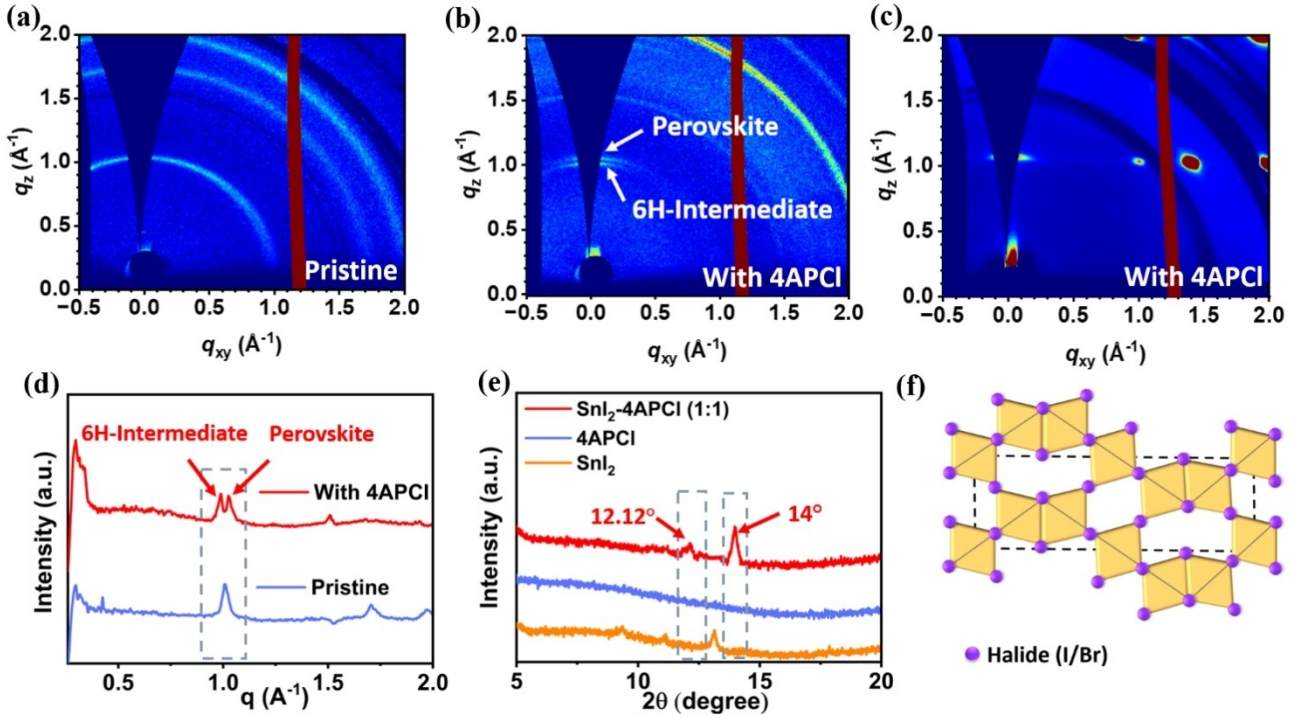

Figure 2. The formation of the 6H-intermediate phase during perovskite film crystallization. GIWAXS patterns at the incident angle of 1° for (a) $FASnI_2Br$, (b) $FASnI_2Br$-4APCl perovskite films during the spin coating process and (c) $FASnI_2Br$-4APCl perovskite film after annealing, respectively. (d) GIWAXS intensity during the spin coating process for the $FASnI_2Br$ and $FASnI_2Br$-4APCl perovskite films. (e) X-ray diffraction patterns of SnI_2-4APCl (1:1) compared to SnI_2 and 4APCl films. (f) Possible arrangements and the connectivity of the SnI_6 octahedra of the 6H-intermediate phase.

perovskites based on high lattice coherency.[52] It is noteworthy that the 6H-intermediate phase was observed only for the $FASnI_2Br$-4APCl perovskite film during the spin coating process. For $FASnI_2Br$-2APCl, $FASnI_2Br$-3APCl, and $FASnI_2Br$-PyCl perovskite films, the 6H-intermediate phase peak was not detected, as explained in Figure S6. This observation is consistent with the electrostatic potential (ESP) analysis in Figures 1C and S1, which demonstrates that the 4APCl molecule exhibits a higher electron density around the nitrogen atom in the pyridine ring compared to the 3APCl, 2APCl, and PyCl molecules. Consequently, 4APCl promotes stronger interactions with the perovskite precursor, which are crucial for facilitating the formation of the 6H-intermediate phase. This, in turn, enables a slower crystallization process for the $FASnI_2Br$-4APCl perovskite films, which was confirmed as follows.

The formation of the 6H-intermediate phase is expected to significantly impact crystallization kinetics. In situ UV/Vis absorption spectroscopy was conducted during the spin coating process in order to investigate the change in crystal growth rate. For the pristine $FASnI_2Br$ and $FASnI_2Br$-4APCl perovskite films, the absorption intensity started to rise and the spectral peak broadened after 50 seconds of spin coating of the perovskite precursor solution, indicating the formation of perovskite crystals (Figures 3a, S7). The absorption intensity at 600 nm was analysed in relation to the spin coating duration, as illustrated in Figure 3b. For the pristine $FASnI_2Br$ perovskite, the absorption intensity quickly reached its maximum level within 1.5 seconds (51.25–52.75 s). In contrast, for the $FASnI_2Br$-4APCl perovskite film, the absorption intensity increased significantly slower within a span of 4.25 seconds (52–56.25 s), indicating a slower crystal growth rate for the $FASnI_2Br$-4APCl perovskites (Figure 3b). Furthermore, the first derivative of the UV/Vis absorption intensity was calculated as shown in Figure 3c. The crystal growth rate of the $FASnI_2Br$-4APCl perovskites was observed to be 0.27 s^{-1}, which is significantly lower than that of $FASnI_2Br$ perovskites (0.76 s^{-1}). These results indicate that the 6H-intermediate phase has the potential to reduce the crystal growth rate of $FASnI_2Br$-4APCl perovskites during the spin coating process, thereby enabling the production of high-quality perovskite films. It is noteworthy to mention that the absorption intensity over time was also measured for 2APCl, 3APCl, and PyCl, as depicted in Figure S7. The extracted intensity at 600 nm indicated the decreased crystal growth of after using 4APCl, 2APCl, 3APCl, and PyCl, compared to the pristine perovskite film shown in Figure S8a. Furthermore, the calculated crystal growth rate depicted in Figure S8b revealed a decrease in crystal growth rate of perovskite film in the following sequence: $FASnI_2Br$ > $FASnI_2Br$-PyCl > $FASnI_2Br$-3APCl > $FASnI_2Br$-2APCl > $FASnI_2Br$-4APCl. These findings are consistent with the results that 4APCl exhibits higher basicity and stronger interactions with the perovskite precursor compared to other aminopyridine isomers.

Furthermore, in situ UV/Vis absorption spectroscopy of the perovskite films during the annealing process was

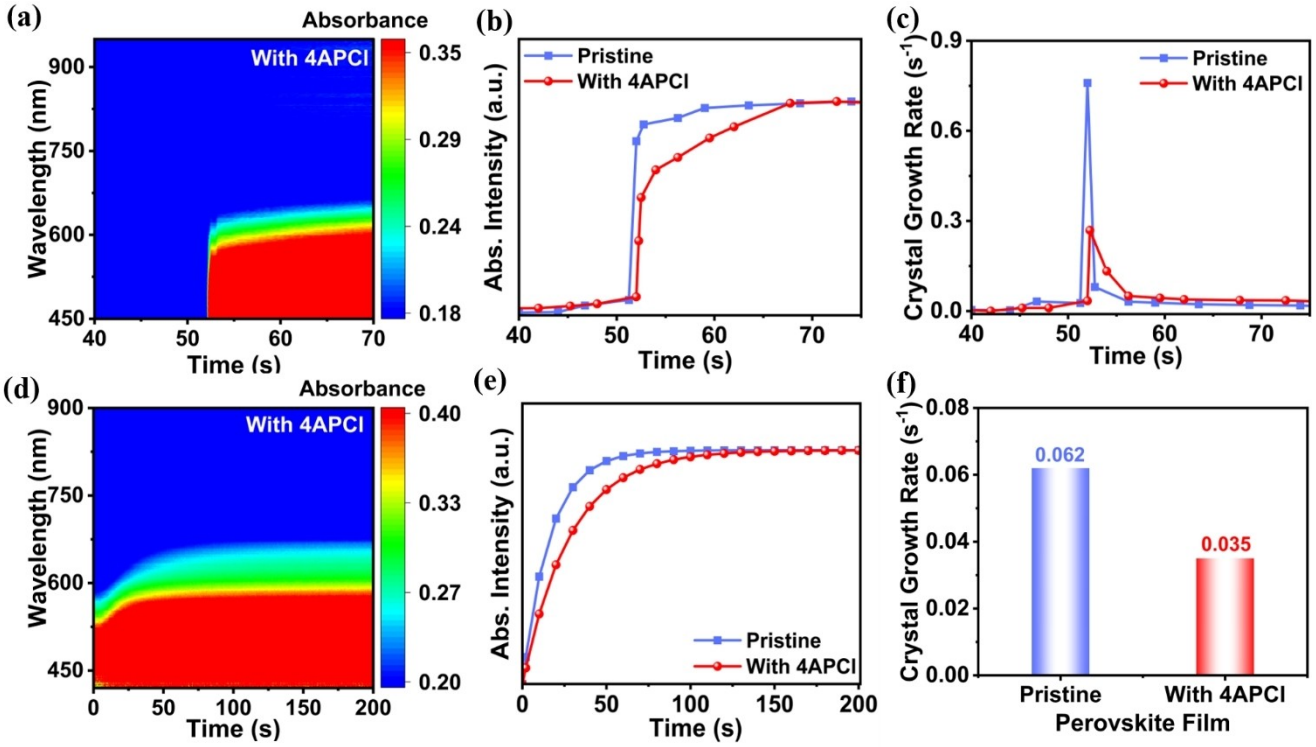

Figure 3. Effect of the 6H-intermediate phase on the crystallization kinetics of the $FASnI_2Br$-4APCl perovskite film. (a) In situ UV/Vis absorption spectra during spin coating process for the $FASnI_2Br$-4APCl perovskite film. (b) Extracted absorption intensity against time of the $FASnI_2Br$ and $FASnI_2Br$-4APCl perovskite films and (c) their corresponding first derivative at 600 nm. (d) In situ UV/Vis absorption spectra during annealing process for the $FASnI_2Br$-4APCl perovskite film. (e) Extracted absorption intensity against time of the $FASnI_2Br$ and $FASnI_2Br$-4APCl perovskite films and (f) their corresponding crystal growth rates at 600 nm.

conducted to provide a deeper understanding of crystal growth kinetics (Figures 3d, S9). The extracted absorption intensity against time indicated the reduction in crystal growth rate in the following order: $FASnI_2Br$ > $FASnI_2Br$-PyCl > $FASnI_2Br$-3APCl > $FASnI_2Br$-2APCl > $FASnI_2Br$-4APCl, as depicted in Figures 3e, S10a. Importantly, the $FASnI_2Br$-4APCl perovskite film with the 6H-intermediate phase exhibited the lowest crystal growth rate ($0.035\ s^{-1}$), compared to the pristine $FASnI_2Br$ perovskite film ($0.062\ s^{-1}$) and other aminopyridine derivatives (Figures 3f, S10b). The results obtained from in situ UV/Vis measurements during the spin coating and annealing processes are consistent, indicating the significant role of the 6H-intermediate phase in retarding the crystal growth of the $FASnI_2Br$-4APCl perovskite films. Notably, a slower crystal growth during spin coating of $FASnI_2Br$-4APCl, compared to pristine $FASnI_2Br$, was clearly visible to the naked eye (Figure S11a). After completing the spin coating process, we observed that the $FASnI_2Br$-4APCl perovskite film exhibited a lighter brown color (Movie S1) compared to the pristine $FASnI_2Br$ film (Movie S2), confirming the slower crystal growth of the $FASnI_2Br$-4APCl film. Furthermore, after 5-minutes of spin coating the perovskite films, pristine $FASnI_2Br$ turned to dark brown color which indicated fast crystallization. In contrast, the $FASnI_2Br$-4APCl perovskite film exhibit lighter brown color (Figure S11b), which prove the slower crystallization process.

The influence of 4APCl, 2APCl, 3APCl and PyCl amounts on the crystal growth rate of the $FASnI_2Br$ perovskite film has been explored. As shown in Figures S12–S15, increasing the amount of 4APCl, 2APCl, 3APCl, or PyCl from 1 mol % to 5 mol % slows down the crystal growth rate gradually. Furthermore, it is evident that 4APCl demonstrates superior ability in reducing the crystal growth rate across various concentrations when compared to 2APCl, 3APCl, and PyCl (Table S2). Compared to the 1 mol % and 2 mol % concentrations, the 5 mol % concentration of 4APCl, 2APCl, 3APCl, or PyCl exhibited the lowest crystal growth rate. However, this significantly lowest growth rate at 5 mol % may be inferior to the film quality due to the unbalanced process between crystal nucleation and growth steps. These observations confirm that although higher additive concentrations can significantly reduce the crystal growth rate, excessive reduction may negatively impact the overall crystallization process and device performance.

Furthermore, the crystallization process was analyzed by the in situ UV/Vis absorption spectra during annealing at various temperatures (60 °C, 70 °C, 80 °C, and 90 °C). As depicted in Figures S16 (a–d) and Figures S16 (e–h), the absorption intensity at 600 nm increases as a function of the annealing time, which is characteristic of the thermally driven crystallization process. We extracted the absorption intensity at 600 nm against the annealing time in order to

quantify the differences in crystallization (Figures S16i and j), and then we fitted the time-dependent curves at 600 nm with a monoexponential function. As shown in Table S3, the crystal growth rate of the tin halide perovskite films with 4APCl exhibits a significant decrease due to the formation of 6H-intermediate phase. Furthermore, as expected, the crystallization process is accelerated at a higher temperature. The crystal growth rate constants under different temperature align well with the Arrhenius equation $k = A\,exp(-E_a/RT)$ (equation S7). As fitted in Figure S16k, the activation energy for crystallization (E_a) of the pristine film was 31.51 kJ/mol. Interestingly, the formation of 6H-intermediate phase induced by 4APCl additive enhanced the activation energy to 39.18 kJ/mol for tin halide perovskite crystallization. The higher activation energy can reduce crystal growth rate, result in the improved crystallization kinetics and superior perovskite films.

In order to investigate the effects of the 6H-intermediate phase on the morphology of $FASnI_2Br$ perovskite film, the scanning electron microscopy (SEM) was measured. As depicted in Figure 4a, the $FASnI_2Br$ perovskite film displayed numerous pinholes, resulting from the rapid crystal growth of $FASnI_2Br$ perovskites. In contrast, the addition of 2 mol % 4APCl to the $FASnI_2Br$ perovskite film resulted in a denser structure, devoid of pinholes and characterized by larger grain sizes. Moreover, increasing the amount of 4APCl to 3 mol % led to a deterioration in morphology and plentiful defects, as illustrated in Figure S17. This indicates that 2 mol % of 4APCl is optimal to form the 6H-intermediate phase for controlling the crystal growth. As a result, the $FASnI_2Br$-4APCl (2 mol %) perovskite film quality was improved. Notably, the X-ray diffraction (XRD) analysis revealed that the XRD intensity of the (100) and (200) peaks was enhanced after inclusion of 2 mol % 4APCl compared to the pristine $FASnI_2Br$ (Figure 4b). Particularly, the utilizing of 4APCl (2 mol %) affords the most intense peak, as shown in Figure S18. Furthermore, the XRD analysis reveals a significant reduction in the full width at half maximum (FWHM) of the diffraction peaks, as shown in Figure S19. It is noteworthy that the reduction in FWHM could be observed across all diffraction peaks of the $FASnI_2Br$-4APCl perovskite film, as presented in Table S4. This observation confirms the superior crystallinity of the $FASnI_2Br$ perovskite film after the inclusion of 4APCl. Additionally, the crystalline size of the $FASnI_2Br$-4APCl perovskite films showed a clear increase to 115.9 nm compared to 96.5 nm for the pristine $FASnI_2Br$ perovskite film (Table S5), which is in line with the SEM results. We calculated the change in lattice strain after inclusion of 4APCl using Williamson-Hall plots (Supplementary Note S1). As indicated in Figure 4c, the strain of the $FASnI_2Br$-4APCl perovskite film was decreased to 0.0013 compared to 0.0016 for the pristine $FASnI_2Br$ perovskite film. The decreased lattice distortion is attributed to the formation of the 6H-intermediate phase, which promotes uniform crystallization in the mixed-halide perovskite phase.[40]

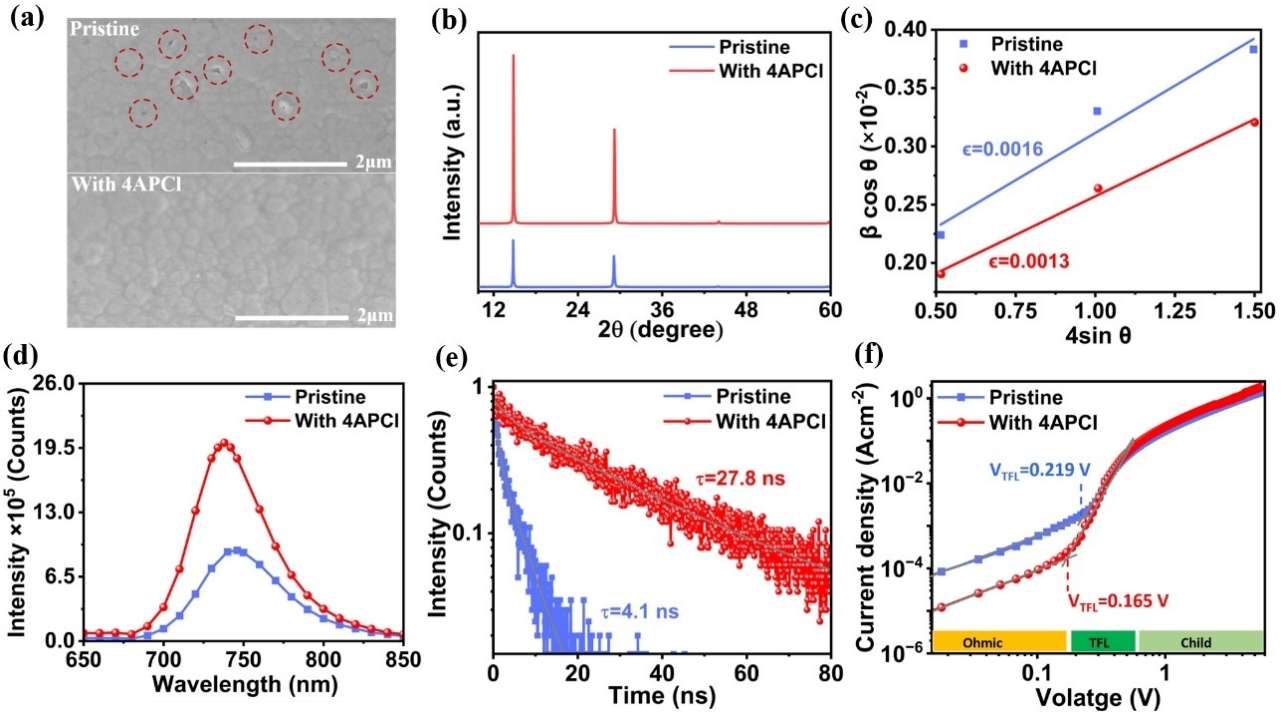

Figure 4. Effect of the 6H-intermediate phase on the morphology, crystalline and optoelectronic properties of the perovskite films. (a) Scanning electron microscope images, (b) X-ray diffraction patterns, (c) Williamson-Hall plots fitting of the $FASnI_2Br$ perovskite film without and with 4APCl (2 mol%), respectively. (d) Steady-state photoluminescence spectra and (e) Time-resolved photoluminescence decay spectra for the $FASnI_2Br$ perovskite film without and with 4APCl (2 mol%). (f) Dark *J–V* curves of the hole only devices based on the $FASnI_2Br$ perovskite film without and with 4APCl (2 mol%).

To investigate the influence of the 6H-intermediate phase on the charge carrier dynamics of the $FASnI_2Br$-4APCl perovskite film, we conducted the steady-state photoluminescence (PL) spectra. As illustrated in Figure 4d, the $FASnI_2Br$-4APCl perovskite film exhibited a stronger PL intensity than the pristine $FASnI_2Br$ film, which indicated suppression of the non-radiative recombination centers. Hence, the V_{oc} loss of the fabricated wide band gap $FASnI_2Br$ based IPVs was expected to decrease. Importantly, the emission peak of $FASnI_2Br$ pristine perovskite film at ~745 nm was blue-shifted to 738 nm for $FASnI_2Br$-4APCl perovskite film, as depicted in Figure 4d. The blue shift ensured the reduction of crystal growth through the formation of the 6H-intermediate phase, thereby enhancing the formation of perovskite films with fewer defects and enhanced quality. We further investigated the charge transfer kinetics using time-resolved photoluminescence (TRPL) measurements for $FASnI_2Br$-4APCl perovskite films. The TRPL analysis shown in Figure 4e revealed that the $FASnI_2Br$-4APCl perovskite film exhibited a significant increase in PL lifetime to 27.8 ns, compared to 4.1 ns for the pristine $FASnI_2Br$ perovskite film. The PL and TRPL results with different concentrations of 4APCl from 1 to 3 mol % indicated that the most pronounced composition of 4APCl was 2 mol % (Figures S20). The enhanced PL intensity with blue shift and prolonged lifetime indicate suppression of the nonradiative recombination channels and reduced trap density. Thus, confirming that the formation of the 6H-intermediate phase during crystallization assisted in controlling the crystal growth of $FASnI_2Br$-4APCl perovskite, which is expected to achieve efficient IPVs.

The preceding analysis suggests that the inclusion of 4APCl facilitated the formation of the 6H-intermediate phase during the crystallization of $FASnI_2Br$-4APCl perovskite films. This could successfully produce high-quality perovskite films with improved crystallinity, less pinholes, fewer defects, a larger grain size, and suppression of the nonradiative recombination channels. Furthermore, the trap states of the $FASnI_2Br$-4APCl perovskite films are expected to be minimized compared to those of the pristine $FASnI_2Br$. To ensure that, the space charge limiting current (SCLC) of hole-only devices was measured with the structure of ITO/PEDOT:PSS/perovskite/PTAA/Ag (Figure 4f). The trap density (N_t) was determined using the equation S6. The trap density of pristine $FASnI_2Br$ perovskite films was 1.49×10^{16} cm^{-3}, while that for the $FASnI_2Br$-4APCl perovskite film decreased to 1.13×10^{16} cm^{-3}. As a result of slower crystal growth, the trap states in the $FASnI_2Br$-4APCl perovskite films can be effectively diminished, leading to superior perovskite films with fewer defects and better quality.

To investigate the oxidation process of Sn^{2+} to Sn^{4+} in the perovskite precursor, X-ray photoelectron spectroscopy (XPS) was performed on $FASnI_2Br$ and $FASnI_2Br$-4APCl perovskite films. As shown in Figure S21, the addition of 4APCl decreased the Sn^{4+}/Sn^{2+} ratio from 54.7 % to 31.8 %. This decrease in Sn^{2+} oxidation can be explained by the strong basicity of 4APCl, which could prevent Sn^{2+} oxidation. Furthermore, the percentage of N1s increased from 15.02 % to 15.54 % (Table S6). This increase in the percentage of N1s proves the interaction between 4APCl and perovskites. The $Cl2p_{3/2}$ and $Cl2p_{1/2}$ peaks were detected in $FASnI_2Br$-4APCl film at 199.3 and 200.9 eV, respectively, which indicate the interaction of 4APCl with the perovskite (Figure S22 and Table S6). Additionally, the observed shifts in Sn3d and I3d for the $FASnI_2Br$-4APCl compared to the pristine $FASnI_2Br$ perovskite film indicates the strong interaction between 4APCl and perovskites (Figure S23). Importantly, the inclusion of 4APCl increased the Sn/I and Sn/Br ratios compared to the pristine perovskite film, as explained in Table S7. This suggests that the formation of the 6H-intermediate phase suppressed the I/Br vacancies in the $FASnI_2Br$-4APCl perovskite film, resulting in lower recombination centers and reduced segregation. Furthermore, energy dispersive X-ray (EDX) and time-of-flight secondary-ion mass spectrometry (TOF-SIMS) spectra were employed to investigate the spatial positions of 4APCl molecules in the perovskite films. As shown in Figure S24, S25 and S26, 4APCl was homogeneously distributed in the perovskite films, thereby facilitating the formation of the 6H-intermediate phase throughout the $FASnI_2Br$ perovskite film.

The noteworthy enhancement in the quality of the $FASnI_2Br$-4APCl perovskite film resulting from the formation of the 6H-intermediate phase suggests enhancing the photovoltaic performance of PSCs. Consequently, we fabricated solar cell devices with the aim of evaluating their indoor photovoltaic performance. Figure 5a presented the cross-sectional SEM images of the fabricated PSCs (ITO/PEDOT:PSS/perovskite/ICBA/BCP/Ag). The spectrum of the indoor light source used in this work is provided in Figure S27. The highest indoor PCE of the devices based on pristine $FASnI_2Br$ was only 15.18 % (Figure 5b). In contrast, the champion indoor PCE for the devices based on $FASnI_2Br$-4APCl was jumped to 21.55 %, with a V_{oc} of 0.721 V, a short-circuit current density (J_{sc}) of 119 $\mu A\,cm^{-2}$, and a fill factor (*FF*) of 0.724. The *J–V* curves and detailed photovoltaic performance using different amounts of 4APCl are given in Figure S28 and Table S8. The improvement in PCE of the $FASnI_2Br$-4APCl based PSCs stemmed from a significant increase in V_{oc}, rising from 0.646 to 0.721 V, alongside an improved *FF* from 0.656 to 0.724. The substantial increase in V_{oc} and *FF* can be attributed to the formation of the 6H-intermediate phase, which exhibits a large number of corner-sharing octahedra that can act as inter-grain growth, thereby facilitating a controlled crystallization process.[52] Thus, the $FASnI_2Br$-4APCl perovskite film was formed with high quality, released strain, reduced defects, resulting in a lower recombination process and enhanced photovoltaic efficiency. Furthermore, the fabricated devices showed a high reproducibility of up to 26 devices, as depicted in Figure S29 and S30. The distribution clearly demonstrates the superiority of the 4APCl-modified devices compared to the pristine ones. Furthermore, the average indoor photovoltaic efficiency for the devices based on $FASnI_2Br$-4APCl (18.89 ± 1.39 %) was also higher than that for the devices based on pristine $FASnI_2Br$ (13.67 ± 1.02 %), as shown in Table S9. The recent advances in

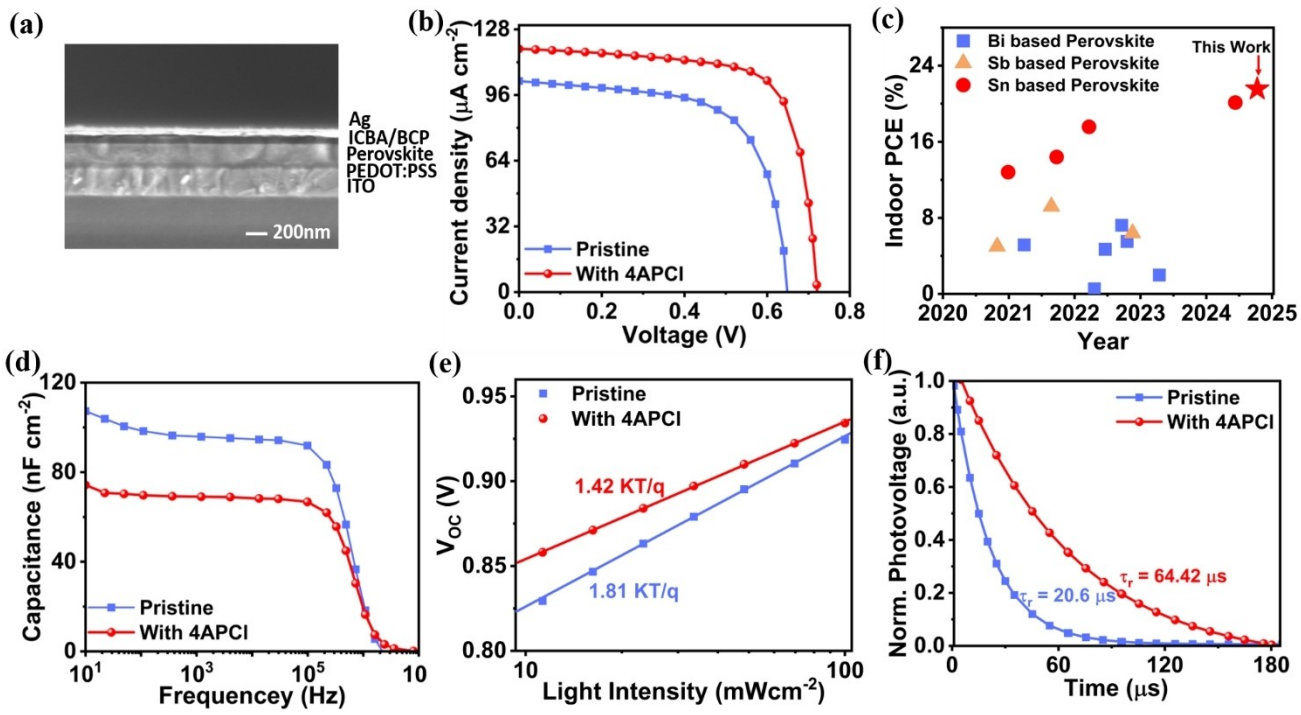

Figure 5. Effect of the 6H-intermediate phase on the indoor photovoltaic performance. (a) Cross-sectional view scanning electron microscope image of the $FASnI_2Br$-4APCl based device. (b) *J–V* curves of the champion devices based on $FASnI_2Br$ and $FASnI_2Br$-4APCl under indoor illumination of 1000 lux. (c) Indoor photovoltaic efficiencies for lead-free perovskite solar cells based on Sn, Bi, and Sb reported in literatures and this work. (d) Admittance spectra, (e) V_{oc} versus light intensity and (f) Transient photovoltage decay profiles of $FASnI_2Br$ and $FASnI_2Br$-4APCl based device.

indoor photovoltaic efficiency of lead-free perovskite solar cells based on Sn, Bi, and Sb are explained in Figure 5c. In this work, we achieved the highest indoor photovoltaic efficiency of 21.55 % for lead-free perovskite solar cells to date (Table S10). The external quantum efficiency (EQE) of the fabricated PSCs is presented in Figure S31. Notably, the EQE response in the wavelength range 300–700 nm was enhanced for the $FASnI_2Br$-4APCl devices compared to the pristine $FASnI_2Br$ devices, indicating improved quality of the $FASnI_2Br$-4APCl perovskite. Furthermore, the integrated current densities calculated from the EQE of the PSCs were consistent with the experimentally obtained J_{sc} values (Figure S31). The forward and reverse scan directions are given in Figure S32. Moreover, the photovoltaic performance under one sun illumination was evaluated, as depicted in Figure S33 and Table S11. The stability of the devices was evaluated under ambient air and continuous indoor light illumination (Figure S34). Despite the rapid degradation of the $FASnI_2Br$ devices upon exposure to air, the $FASnI_2Br$-4APCl devices exhibited enhanced stability, maintaining approximately 85 % of their initial efficiency after a duration of 100 hours of air exposure (Figure S34a). Furthermore, the encapsulated $FASnI_2Br$-4APCl devices exhibited superior stability under continuous indoor light illumination (~1000 lux), maintaining 93 % of their initial efficiency, in contrast to 84 % for the pristine $FASnI_2Br$ devices as depicted in Figure S34b. This enhanced stability can be attributed to the high-quality $FASnI_2Br$-4APCl perovskite film and the substantial reduction in lattice strain and defects.

In order to gain a deeper understanding of the effects of the 6H-intermediate phase on the charge transport and recombination dynamics of the fabricated $FASnI_2Br$-4APCl PSCs, we conducted measurements of the capacitance versus frequency (*C–f*) curves. As depicted in Figure 5d, the capacitance of the $FASnI_2Br$-4APCl device was significantly lower than that of the $FASnI_2Br$ device, indicating a reduced defect density in the $FASnI_2Br$-4APCl perovskite film. Moreover, the built-in potential (V_{bi}) in both pristine and target devices was obtained from Mott-Schottky curves (Figure S35). The V_{bi} increased from 0.846 V in the pristine device to 0.914 V in the target device, signifying an enhanced driving force for charge separation and reduced trap-induced nonradiative recombination in the target device. This directly contributed to the prominently enhanced V_{oc} of the $FASnI_2Br$-4APCl based PSCs. We also measured the dependence of V_{oc} on various light intensities (Figure 5e), following the relationship of $V_{oc}\infty$ (nkT/q) ln (I_{light}), where n is the slope, k is the Boltzmann constant, T is the temperature and q is the elementary charge, respectively. The $FASnI_2Br$-4APCl device showed a lower n value (1.42) compared to that (1.81) of the pristine device, suggesting the reduction of trap-assisted recombination in the devices containing 6H-intermediate phase. Furthermore, the $FASnI_2Br$-4APCl PSCs exhibited a lower dark current density 3.45×10^{-8} mA cm^{-2} compared to 9.69×10^{-6} mA cm^{-2}

for the pristine $FASnI_2Br$ PSCs (Figure S36). This substantial reduction in leakage current suggests fewer defect states and diminished carrier recombination in the $FASnI_2Br$-4APCl device.[19] Additionally, we performed a transient photovoltage decay analysis, which provides insights into the carrier recombination mechanisms. A more rapid photovoltage decay indicates accelerated recombination. As depicted in Figure 5f, the recombination lifetime (τ_r) of the $FASnI_2Br$-4APCl PSCs was significantly delayed to 64.42 μs, as compared to 20.6 μs of pristine $FASnI_2Br$ PSCs, which indicates a significant decrease in the recombination rate after introducing the 6H-intermediate phase.

The electrochemical impedance spectroscopy (EIS) was also analyzed under dark conditions. From the EIS curve, $FASnI_2Br$-4APCl PSCs exhibited larger recombination resistance than $FASnI_2Br$ PSCs, demonstrating that non-radiative recombination was obviously suppressed in the $FASnI_2Br$-4APCl devices (Figure S37). The aforementioned findings regarding the device physics are completely consistent with the characterization results of the perovskite films. Thereby, this demonstrates the successful retarding of the crystallization process via the 6H-intermediate phase formation. Furthermore, the impact of the 6H-intermediate phase on the recombination dynamics within the devices was also examined by analyzing the dependence of J_{sc} on various light intensities. The relationship between J_{sc} and light intensity is described as $J_{sc} \propto P^{\alpha}$, where the exponent α deviating from 1 implies the extent of bimolecular recombination. As shown in Figure S38, the extracted α values were 0.99 and 0.96 for the devices with $FASnI_2Br$-4APCl and $FASnI_2Br$, respectively, indicating that the bimolecular recombination was reduced after formation of the 6H-intermediate phase.

Conclusion

To summarize, we developed a straightforward and robust strategy to regulate the crystallization kinetics of tin halide perovskites via the formation of the 6H-intermediate phase. Firstly, the positive mesomeric interaction (+M) stabilized the negative charge on the nitrogen of the pyridine ring of 4APCl, which afforded strong interaction with the perovskite precursor, thereby establishing the 6H-intermediate phase during the formation of perovskite films. Subsequently, the GIWAXS measurements revealed that the 6H-intermediate perovskite phase was formed after the inclusion of 4APCl. This is the first time that the 6H-intermediate phase was observed during the crystallization process of tin halide perovskites. Thus, in situ UV/Vis absorption measurements during the spin coating and annealing processes confirmed that the $FASnI_2Br$-4APCl perovskite film enabled a slower crystallization rate after introducing the 6H-intermediate phase. As a result, high-quality $FASnI_2Br$-4APCl perovskite films were produced, featuring a notable reduction in defects, larger grain sizes, and enhanced surface morphology. The fabricated $FASnI_2Br$-4APCl indoor photovoltaics achieved an impressive PCE of 21.55 % under 1000 lux illumination, which is the highest reported value for lead-free perovskite IPVs to date. Our emphasis on the formation of the 6H-intermediate phase will open up new avenues for designing tin halide perovskites for efficient IPVs.

Acknowledgements

This work was supported by the National Key R&D Program of China (2024YFB3614300) and the National Natural Science Foundation of China (22179131), the Fundamental Research Funds for the Central Universities, and the University of Chinese Academy of Sciences. We thank Dr. Yao Zhao from the Huairou Research Center, Institute of Chemistry, Chinese Academy of Sciences, for the ToF-SIMS experiments and data analysis. A portion of this work is based on the data obtained at BSRF-1W1A. The authors gratefully acknowledge the cooperation of the beamline scientists at BSRF-1W1A beamline.

Conflict of Interest

The authors declare no competing financial interest.

Data Availability Statement

The data that support the findings of this study are available from the corresponding author upon reasonable request.

Keywords: indoor photovoltaic · lead-free perovskite · crystal growth · 6H-intermediate phase · mesomeric interaction effect

[1] Y. Ren, D. Zhang, J. Suo, Y. Cao, F. T. Eickemeyer, N. Vlachopoulos, S. M. Zakeeruddin, A. Hagfeldt, M. Grätzel, *Nature* **2023**, *613*, 60–65.
[2] J. Min, S. Demchyshyn, J. R. Sempionatto, Y. Song, B. Hailegnaw, C. Xu, Y. Yang, S. Solomon, C. Putz, L. Lehner, J. F. Schwarz, C. Schwarzinger, M. Scharber, E. S. Sani, M. Kaltenbrunner, W. Gao, *Nat. Electron.* **2023**, *6*, 630–641.
[3] Y. Cui, Y. Wang, J. Bergqvist, H. Yao, Y. Xu, B. Gao, C. Yang, S. Zhang, O. Inganäs, F. Gao, J. Hou, *Nat. Energy* **2019**, *4*, 768–775.
[4] R. Haight, W. Haensch, D. Friedman, *Science* **2016**, *353*, 124–125.
[5] C. H. Chen, Z. H. Su, Y. H. Lou, Y. J. Yu, K. L. Wang, G. L. Liu, Y. R. Shi, J. Chen, J. J. Cao, L. Zhang, X.-Y Gao, Z.-K Wang, *Adv. Mater.* **2022**, *34*, 2200320.
[6] Y. Du, Q. Tian, X. Chang, J. Fang, X. Gu, X. He, X. Ren, K. Zhao, S Liu, *Adv. Mater.* **2022**, *34*, 2106750.
[7] K. L. Wang, H. Lu, M. Li, C. H. Chen, D. Bo Zhang, J. Chen, J. J. Wu, Y. H. Zhou, X. Q. Wang, Z. H. Su, Y. R. Shi, Q. S. Tian, Y. X. Ni, X. Y. Gao, S. M. Zakeeruddin, M. Grätzel, Z.-K. Wang, L. S. Liao, *Adv. Mater.* **2023**, *35*, 2210106.
[8] B. T. Muhammad, S. Kar, M. Stephen, W. L. Leong, *Mater. Today Energy* **2022**, *23*, 100907.
[9] Z. Guo, A. K. Jena, T. Miyasaka, *ACS Energy Lett.* **2022**, *8*, 90–95.

[10] C. Zhang, C. Liu, Y. Gao, S. Zhu, F. Chen, B. Huang, Y. Xie, Y. Liu, M. Ma, Z. Wang, S. Wu, R. E. Schropp, Y Mai, *Adv. Sci* **2022**, *9*, 2204138.
[11] N. Lamminen, G. K. Grandhi, F. Fasulo, A. Hiltunen, H. Pasanen, M. Liu, B. Al-Anesi, A. Efimov, H. Ali-Löytty, K. Lahtonen, P. Mäkinen, A. Matuhina, A. B. Muñoz-García, M. Pavone, P. Vivo, *Adv. Energy Mater.* **2022**, *13*, 2203175.
[12] V. Pecunia, L. G. Occhipinti, R. Z. Hoye, *Adv. Energy Mater.* **2021**, *11*, 2100698.
[13] D. Dou, H. Sun, C. Li, S. Gan, L. Li, *Adv. Funct. Mater.* **2024**, *34*, 2314398.
[14] W. Lu, Z. Li, M. Feng, J. Wei, X. Wen, X. An, Z. Wei, Y. Lin, J.-S. Hu, D.-J. Xue, *Angew. Chem. Int. Ed.* **2024**, e202413429.
[15] C. Fei, A. Kuvayskaya, X. Shi, M. Wang, Z. Shi, H. Jiao, T. J. Silverman, M. Owen-Bellini, Y. Dong, Y. J. S. Xian, *Science* **2024**, *384*, 1126–1134.
[16] B. Zhang, Z. Hu, J. Su, Z. Gong, X. Guo, X. Chen, Y. Yang, Z. Lin, L. Ding, Y. Hao, J. Chang, *Angew. Chem. Int. Ed.* **2024**, e202413550.
[17] E. Hou, J. Chen, J. Luo, Y. Fan, C. Sun, Y. Ding, P. Xu, H. Zhang, S. Cheng, X. Zhao, L. Xie, J. Yan, C. Tian, Z. Wei, *Angew. Chem. Int. Ed.* **2024**, *136*, e202402775.
[18] Q. Ma, Y. Wang, L. Liu, P. Yang, W. He, X. Zhang, J. Zheng, M. Ma, M. Wan, Y. Yang, C. Zhang, T. Mahmoudi, S. Wu, C. Liu, Y. B. Hahn, Y. Mai, *Energy Environ. Sci.* **2024**, *17*, 1637–1644.
[19] Y. Li, T. Nie, X. Ren, Y. Wu, J. Zhang, P. Zhao, Y. Yao, Y. Liu, J. Feng, K. Zhao, W. Zhang, S. Liu, *Adv. Mater.* **2024**, *36*, 2306870.
[20] Q. Ma, M. Ma, L. Liu, P. Yang, W. He, X. Zhang, J. Zheng, C. Zhang, C. Liu, S. Wu, Y. Wang, Y. Mai, *Device* **2023**, *1*, 100174.
[21] M. Lee, J. Lim, E. Choi, A. M. Soufiani, S. Lee, F. J. Ma, S. Lim, J. Seidel, D. H. Seo, J. S. Park, W. Lee, J. Lim, R. F. Webster, J. Kim, D. Wang, M. A. Green, D. Kim, J. H. Noh, X. Hao, J. S. Yun, *Adv. Mater.* **2024**, *36*, 2402053.
[22] Y. Wang, T. Yang, W. Cai, P. Mao, Y. Yang, N. Wu, C. Liu, S. Wang, Y. Du, W. Huang, G. Zhao, Z. Ding, N. Yuan, J. Ding, Y. Zhong, S. Liu, K. Zhao, *Adv. Mater.* **2024**, *36*, 2312014.
[23] M. Ren, X. Qian, Y. Chen, T. Wang, Y. Zhao, *J. Hazard. Mater.* **2022**, *426*, 127848.
[24] M. Yang, T. Tian, Y. Fang, W.-G. Li, G. Liu, W. Feng, M. Xu, W.-Q Wu, *Nat. Sustain.* **2023**, *6*, 1455–1464.
[25] G. Li, Y. T. Liu, F. Yang, M. Li, Z. Zhang, J. Pascual, Z. K. Wang, S. Z. Wei, X. Y. Zhao, H. R. Liu, J.-B. Zhao, C.-T. Lin, J.-M. Li, Z. Li, A. Abate, I. Cantone, *Adv. Mater.* **2024**, *36*, 2306860.
[26] W. Ke, M.G Kanatzidis, *Nat. Commun* **2019**, *10*, 965.
[27] M. Pitaro, E. K. Tekelenburg, S. Shao, M. A. Loi, *Adv. Mater.* **2022**, *34*, 2105844.
[28] A. K. Baranwal, H. Bi, G. Kapil, T. Kitamura, L. Wang, J. Liu, Q. Shen, S. Hayase, *ACS Energy Lett.* **2024**, *9*, 4119–4126.
[29] P. Li, X. Cao, J. Li, B. Jiao, X. Hou, F. Hao, Z. Ning, Z. Bian, J. Xi, L. Ding, Z. Wu, *Nano-Micro Lett.* **2023**, *15*, 167.
[30] T. Wang, J. Cao, F. Yan, *Matter* **2024**, *7*, 2755–2757.
[31] D. Kim, M. Safdari, S. W. Lee, C. Liu, Y. Yang, S. D. Namgung, E. H. Sargent, M. C. Hersam, D.-H. Kim, M. G. Kanatzidis, *ACS Energy Lett.* **2023**, *8* 5221–5228.
[32] M. H. Li, X. Gong, S. Wang, L. Li, J. Fu, J. Wu, Z.a. Tan, J. S. Hu *Angew. Chem. Int. Ed.* **2024**,, *63*, e202318591.
[33] G. Nasti, M. H. Aldamasy, M. A. Flatken, P. Musto, P. Matczak, A. Dallmann, A. Hoell, A. Musiienko, H. Hempel, E. Aktas, D. Girolamo, J. Pascual, G. Li, M. Li, L. Vittoria, M. Paola, D. Veneri, A. Abate, *ACS Energy Lett.* **2022**, *7*, 3197–3203.
[34] E. Jokar, C.-H. Chien, A. Fathi, M. Rameez, Y.-H. Chang, E. W.-G. Diau, *Energy Environ. Sci.* **2018**, *11*, 2353–2362.
[35] Y. Yang, J. Wu, X. Wang, Q. Guo, X. Liu, W. Sun, Y. Wei, Y. Huang, Z. Lan, M. Huang, J. Lin, H. Chen, Z. Wei, *Adv. Mater.* **2020**, *32*, 1904347.
[36] N. Wu, T. Yang, Z. Wang, Y. Wu, Y. Wang, C. Ma, H. Li, Y. Du, D. Zhao, S. Wang, P. Liu, W. Huang, X. Ren, S. Liu, K. Zhao, *Adv. Mater.* **2023**, *35*, 2304809.
[37] C. Liu, T. Yang, W. Cai, Y. Wang, X. Chen, S. Wang, W. Huang, Y. Du, N. Wu, Z. Wang, Y. Yang, J. Feng, T. Niu, Z. Ding, K. Zhao, *Adv. Mater.* **2024**, *36*, 2311562.
[38] H. Zhang, W. Xiang, X. Zuo, X. Gu, S. Zhang, Y. Du, Z. Wang, Y. Liu, H. Wu, P. Wang, Q. Cui, H. Su, Q. Tian, S. Liu, *Angew. Chem. Int. Ed.* **2023**, *135*, e202216634.
[39] G. Li, Z. Su, M. Li, F. Yang, M. H. Aldamasy, J. Pascual, F. Yang, H. Liu, W. Zuo, D. Girolamo, Z. Iqbal, G. Nasti, A. Dallmann, X. Gao, Z. Wang, M. A. Abate, *Adv. Energy Mater.* **2021**, *11*, 2101539.
[40] X. Li, Y. Li, Y. Feng, J. Qi, J. Shen, G. Shi, S. Yang, M. Yuan, T. He, *Adv. Mater.* **2024**, *36*, 2401103.
[41] Q. Ye, W. Hu, J. Zhu, Z. Cai, H. Zhang, T. Dong, B. Yu, F. Chen, X. Wei, B. Yao, W. Dou, Z. Fang, F. Ye, Z. Liu, T. Li, *Energy Environ. Sci.* **2024**, *17*, 5866–5875.
[42] G. Liu, X. Jiang, W. Feng, G. Yang, X. Chen, Z. Ning, W. Q. Wu, *Angew. Chem. Int. Ed.* **2023**, *62*, e202305551.
[43] W.-F. Yang, J.-J. Cao, C. Dong, M. Li, Q.-S. Tian, Z.-K. Wang, L.-S. Liao, *Appl. Phys. Lett.* **2021**, *118*, 023501.
[44] W.-F. Yang, J.-J. Cao, J. Chen, K.-L. Wang, C. Dong, Z.-K. Wang, L.-S. Liao, *Sol. RRL* **2021**, *5*, 2100713.
[45] J.-J. Cao, Y.-H. Lou, W.-F. Yang, K.-L. Wang, Z.-H. Su, J. Chen, C.-H. Chen, C. Dong, X.-Y. Gao, Z.-K. Wang, *J. Chem. Eng.* **2022**, *433*, 133832.
[46] Z. Gao, J. Wang, H. Xiao, M. Abdel-Shakour, T. Liu, S. Zhang, J. Huang, D. J. Xue, S. Yang, X. Meng, *Adv. Mater.* **2024**, *36*, 2403413.
[47] W. F. Yang, F. Igbari, Y. H. Lou, Z. K. Wang, L. S. Liao, *Adv. Energy Mater.* **2020**, *10*, 1902584.
[48] H. Liu, Z. Zhang, W. Zuo, R. Roy, M. Li, M. M. Byranvand, M. Saliba, *Adv. Energy Mater.* **2023**, *13*, 2202209.
[49] J. Hong, C. Kang, R. Huang, Z. Wu, L. Li, X. Li, H. Rao, Z. Pan, X. Zhong, *Adv. Funct. Mater.* **2024**, *34*, 2405374.
[50] J. Essery, K. Schofield, *J. Chem. Soc.* **1961**, 3939–3953.
[51] C. Cumper, A. Singleton, *J. Chem. Soc. B* **1967**, 1096–1099.
[52] H. Kim, S.-M. Yoo, B. Ding, H. Kanda, N. Shibayama, M. A. Syzgantseva, F. F. Tirani, P. Schouwink, H. J. Yun, B. Son, Y. Ding, B.-S Kim, Y. Y. Kim, J. Park, O. A. Syzgantseva, N. J. Jeon, P. J. Dyson, M. K. Nazeeruddin, *Nat. Commun* **2024**, *15*, 5632.
[53] O. E. Solis, M. Mínguez-Avellán, P. F. Betancur, R. I. Sánchez-Alarcón, I. Rodriguez, J. P. Martínez-Pastor, T. S. Ripolles, R. Abargues, P. P. Boix, *ACS Energy Lett.* **2024**, *9*, 5288–5295.
[54] H. Dong, C. Ran, W. Gao, N. Sun, X. Liu, Y. Xia, Y. Chen, W Huang, *Adv. Energy Mater.* **2022**,*12*, 2102213.
[55] Y. Zhang, C. Li, H. Zhao, Z. Yu, X. Tang, J. Zhang, Z. Chen, J. Zeng, P. Zhang, L. Han, H. Chen, *Nat. Commun* **2024**, *15*, 6887.
[56] S. Hu, J. A. Smith, H. J. Snaith, A. Wakamiya, *Precis. Chem.* **2023**, *1*, 69–82.
[57] X. Jiang, H. Li, Q. Zhou, Q. Wei, M. Wei, L. Jiang, Z. Wang, Z. Peng, F. Wang, Z. Zang, K. Xu, Y. Hou, S. Teale, W. Zhou, R. Si, X. Gao, E. H. Sargent, Z. Ning, *J. Am. Chem. Soc.* **2021**, *143*, 10970–10976.
[58] T. Nakamura, T. Handa, R. Murdey, Y. Kanemitsu, A. Wakamiya, *ACS Appl. Electron. Mater.* **2020**, *2*, 3794–3804.
[59] K. Orie, R. Duru, R. Ngochindo, *Am j Heterocycl Chem* **2021**, *7*, 11–25.
[60] J. D. Lee, *Concise inorganic chemistry*, John Wiley & Sons, **2008**.

[61] P. Rotering, L. F. Wilm, J. A. Werra, F. Dielmann, *Chem. Eur. J.* **2020**, *26*, 406–411.
[62] J. Clayden, N. Greeves, S. Warren, P. Wothers, *J Organic Chemistry* **2012**, 339–360.
[63] F. W. Askar, N. K. Abood, N. A.-A. Jinzeel, M.S Falih, *Irq. Nat. J. Chem.* **2013**, *13*, 453–465.
[64] S. A. Ali, A. H. Jabbir, R. A. Mohsie, *Int J Curr Microbiol Appl Sci* **2016**, *5*, 75–83.
[65] Y. Buyukmurat, S. Akyuz, *J. Mol. Struct.* **2003**, *651*, 533–539.
[66] Y. Chen, Y. Ma, Q. He, Q. Han, Q. Zhang, Q. Chen, *cellulose* **2019**, *26* 5033–5049.
[67] P. Gratia, I. Zimmermann, P. Schouwink, J.-H. Yum, J.-N. Audinot, K. Sivula, T. Wirtz, M. K. Nazeeruddin, *ACS Energy Lett.* **2017**, *2*, 2686–2693.
[68] M. Qin, K. Tse, T–K. Lau, Y. Li, C.-J. Su, G. Yang, J. Chen, J. Zhu, U.-S. Jeng, G. Li, H. Chen, X. Lu, *Adv. Mater.* **2019**, *31*, 1901284.

Manuscript received: November 5, 2024
Accepted manuscript online: February 22, 2025
Version of record online: ■■, ■■

Research Article

Indoor Photovoltaics

M. Abdel-Shakour, J. Wang, J. Huang, Z. Gao, Y. Pan, X. Meng* — **e202421547**

6H-Intermediate Phase Enabled Slow Crystal Growth of Tin Halide Perovskites for Indoor Photovoltaics

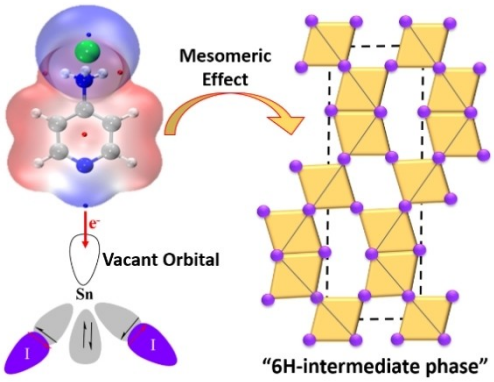

We controlled the crystallization kinetics of $FASnI_2Br$ perovskite via the formation of the 6H-intermediate phase, supported by the mesomeric (+M) interaction effect of 4-aminopyridine hydrochloride (4APCl) in the perovskite precursor.

High-quality $FASnI_2Br$ perovskite films were obtained with reduced defects, which resulted in an efficiency of 21.55% under indoor illumination at 1000 lux.